Monthly Notices of the ROYAL ASTRONOMICAL SOCIETY

MNRAS **514,** 1706–1719 (2022) https://doi.org/10.1093/mnras/stac1441
Advance Access publication 2022 May 30

Stellar kinematics of dwarf galaxies from multi-epoch spectroscopy: application to Triangulum II

Rachel Buttry [1]★ Andrew B. Pace [1] Sergey E. Koposov [1,2,3] Matthew G. Walker [1] Nelson Caldwell,[4] Evan N. Kirby,[5,6] Nicolas F. Martin [7,8] Mario Mateo,[9] Edward W. Olszewski,[10] Else Starkenburg,[11] Carles Badenes[12] and Christine Mazzola Daher [12]

[1]*McWilliams Center for Cosmology, Carnegie Mellon University, 5000 Forbes Ave, Pittsburgh, PA 15213, USA*
[2]*Institute for Astronomy, University of Edinburgh, Royal Observatory, Blackford Hill, Edinburgh EH9 3HJ, UK*
[3]*Institute of Astronomy, University of Cambridge, Madingley Rd, Cambridge CB3 0HA, UK*
[4]*Center for Astrophysics | Harvard & Smithsonian, 60 Garden Street, Cambridge, MA 02138, USA*
[5]*Department of Astronomy, California Institute of Technology, 1200 E. California Blvd., MC 249-17, Pasadena, CA 91125, USA*
[6]*Department of Physics and Astronomy, University of Notre Dame, 225 Nieuwland Science Hall, Notre Dame, IN 46556, USA*
[7]*Observatoire astronomique de Strasbourg, Université de Strasbourg, CNRS, UMR 7550, 11 rue de l'Université, F-67000 Strasbourg, France*
[8]*Max-Planck-Institut für Astronomie, Königstuhl 17, D-69117 Heidelberg, Germany*
[9]*Department of Astronomy, University of Michigan, Ann Arbor, MI 48109, USA*
[10]*Steward Observatory, The University of Arizona, 933 N. Cherry Avenue, Tucson, AZ 85721, USA*
[11]*Kapteyn Astronomical Institute, University of Groningen, Postbus 800, NL-9700 AV, Groningen, the Netherlands*
[12]*Department of Physics and Astronomy and Pittsburgh Particle Physics, Astrophysics and Cosmology Center (PITT PACC), University of Pittsburgh, 3941 O'Hara Street, Pittsburgh, PA 15260, USA*

Accepted 2022 May 14. Received 2022 May 13; in original form 2021 August 25

ABSTRACT

We present new MMT/Hectochelle spectroscopic measurements for 257 stars observed along the line of sight to the ultrafaint dwarf galaxy Triangulum II (Tri II). Combining results from previous Keck/DEIMOS spectroscopy, we obtain a sample that includes 16 likely members of Tri II, with up to 10 independent redshift measurements per star. To this multi-epoch kinematic data set, we apply methodology that we develop in order to infer binary orbital parameters from sparsely sampled radial velocity curves with as few as two epochs. For a previously identified (spatially unresolved) binary system in Tri II, we infer an orbital solution with period $296.0^{+3.8}_{-3.3}$ d, semimajor axis $1.12^{+0.41}_{-0.24}$ au, and systemic velocity -380.0 ± 1.7 km s^{-1} that we then use in the analysis of Tri II's internal kinematics. Despite this improvement in the modelling of binary star systems, the current data remain insufficient to resolve the velocity dispersion of Tri II. We instead find a 95 per cent confidence upper limit of $\sigma_v \lesssim 3.4$ km s^{-1}.

Key words: binaries: spectroscopic – galaxies: kinematics and dynamics.

1 INTRODUCTION

Dwarf galaxies are of great importance for astrophysics. From a galaxy formation perspective, dwarf galaxies are among the oldest and least chemically evolved objects (Mateo 1998; Tolstoy, Hill & Tosi 2009; McConnachie 2012). From a dark matter perspective, they include the most dark matter dominated systems known, with published dynamical mass-to-light ratios reaching as high as 10^4 in solar units (and references therein Simon 2019). In this vein, dwarf galaxies are believed to be key components in unpacking the mystery of dark matter, as they probe the small-scale structure (< 1 Mpc) regime of ΛCDM cosmology (Bullock & Boylan-Kolchin 2017).

In order to place dwarf galaxies into their proper cosmological context, we must obtain accurate estimates of their dark matter content. The simplest dynamical mass estimators, based on the assumption of dynamic equilibrium, are functions of the effective radius and line-of-sight velocity dispersion measured for the stellar component (e.g. Illingworth 1976; Walker et al. 2009; Wolf et al. 2010; Errani, Peñarrubia & Walker 2018). However, measurements of the stellar velocity dispersion can be challenging. One reason is the small number and low luminosities of stellar tracers in especially the 'ultrafaint' dwarf galaxies. Another challenge is the existence of unresolved binary stars, whose orbital motions add a time-dependent component to the velocities measured for individual stars, and – if unaccounted for – can thereby inflate measurements of dwarf galaxy velocity dispersions. Binary orbital motions alone can generate apparent velocity dispersions of a few km s^{-1} (McConnachie & Côté 2010). While this effect is negligible for the more luminous dwarf spheroidals, which have intrinsic velocity dispersions of $\sim$10 km s^{-1} (Olszewski, Pryor & Armandroff 1996), it can potentially contribute significantly to the $\lesssim 3$ km s^{-1} dispersions observed for the least luminous galaxies (McConnachie & Côté 2010; Minor et al. 2010).

Various strategies have been used to account for the effect of binary stars on velocity dispersions and the dynamical masses derived therefrom. When multi-epoch spectroscopy is available, one can identify probable binary systems via their observed accelerations (e.g. Olszewski et al. 1996; Koposov et al. 2011; Martinez et al. 2011; Minor et al. 2019); indeed modelling of multi-epoch spectroscopic

★ E-mail: rbuttry@andrew.cmu.edu

data sets for luminous dwarf spheroidals suggests typical binary fractions near ∼ 50 per cent (Minor 2013; Spencer et al. 2017, 2018), consistent with studies of Galactic binaries that indicate relatively high multiplicity fractions at low metallicity (Badenes et al. 2018). In some cases, the removal of suspected binary stars has a significant impact on the measured velocity dispersion (e.g. Kirby et al. 2017; Venn et al. 2017).

The Triangulum II (Tri II) ultrafaint dwarf galaxy provides an interesting case study. The original kinematic study of Tri II, based on single-epoch spectroscopy of six member stars, measured a velocity dispersion of $5.1^{+4.0}_{-1.4}$ km s^{-1}, suggesting a dynamical mass-to-light ratio of 3600^{+3500}_{-2100} in solar units, and an extremely high dark matter density of $4.8^{+8.1}_{-3.5}$ M$_\odot$ pc^{-3} (Kirby et al. 2015). An independent study by Martin et al. (2016) obtained a spectroscopic sample of 13 member stars, finding complicated kinematics in which a central velocity dispersion of $\sigma_v = 4.4^{+2.8}_{-2.0}$ km s^{-1} gives way to a larger value of $14.1^{+5.8}_{-4.2}$ km s^{-1} at a large radius. Both studies found evidence for non-zero metallicity dispersion, supporting the conclusion that Tri II is a dwarf galaxy embedded in a massive dark matter halo, and not a self-gravitating star cluster.

However, follow-up spectroscopy soon provided a time domain and revealed the presence of at least one star with significant velocity variability. From high-resolution spectra obtained primarily to analyse chemical abundances, Venn et al. (2017) measured a change in velocity for one star (*Star46*) of ∼25 km s^{-1} with respect to the initial epoch measured by Martin et al. (2016). Kirby et al. (2017) added additional epochs for this star, independently confirming its velocity variability and finding that, when they excluded the likely binary from their analysis, the velocity dispersion was unresolved. These circumstances leave the case for a dominant dark matter halo in Tri II resting on the indirect argument provided by its metallicity spread (Venn et al. 2017).

Here, we add to the saga of Tri II in two ways. First, we present new spectroscopic data acquired with the Hectochelle spectrograph at the 6.5-m MMT. Secondly, we combine with the previously published spectroscopic data in order to obtain a multi-epoch data set that then lets us model the orbital parameters of the likely binary star. Our orbital solution includes an inference for the binary system's centre-of-mass motion, allowing us properly to include this star in our analysis of Tri II's stellar kinematics.

To date, only one star system within a dwarf spheroidal galaxy has a full orbital solution, based on 34 independent velocity measurements taken over a 2-yr baseline (Koch et al. 2014). Here, we develop methodology for inferring orbital solutions with as few as two velocity epochs. The problem of finding orbital parameters for a binary system given a small number of radial velocity (RV) measurements has been undertaken previously by Price-Whelan et al. (2017) to create *the JOKER*. Like *the JOKER*, the binary model, we present in this paper takes the approach of performing rejection sampling with likelihood function marginalized over some orbital parameters. However, our method has the added modifications, such as the marginalization over inclination rather than semi-amplitude (allowing for the calculation of semimajor axis), the ability to take non-trivial priors over binary parameters, and using parameter samples for hierarchical models of binary populations.

In the next section, we discuss the MMT and Keck catalogs used in this analysis, as well as the calculation of a zero-point correction between the two instruments. In Section 3, we present our methodology for the modelling of binary and non-binary star systems, as well as the galaxy kinematics. We then detail the resulting orbital parameter for the Tri II binary system and the overall Tri II kinematics in Section 4. Lastly, we discuss the findings from our work in Section 5 and we suggest a hierarchical model building off the methods used.

2 DATA

2.1 MMT Hectochelle

During 2015 December and 2016 October–November, we acquired new spectra of stars in Tri II using the Hectochelle spectrograph (Szentgyorgyi et al. 2011) at the 6.5-m MMT Observatory on Mt. Hopkins, Arizona. Hectochelle deploys up to 240 optical fibers, each with aperture 1.5 arcsec, over a field of diameter 1°. We observed using the 'RV31' filter, isolating the wavelength range of 5150–5300 at resolution $\mathcal{R} \approx 34\,000$.

We observed five different Hectochelle fiber configurations, each centred on the published centre of Tri II, allowing us to observe up to ∼500 unique targets, with many stars included in multiple targeting configurations.

To clean the overwhelming contamination from foreground Milky Way stars, we rely on narrow-band, metallicity sensitive CaHK observations of Tri II. The observations follow a similar strategy and goal as presented by Starkenburg et al. (2017) in the Pristine survey but correspond to a single CFHT MegaCam field centred on Tri II. The field covers the full extent of Tri II and the integration amount to 4800 s in total from the CaHK images. Additional observations were also obtained in the MegaCam g and i bands (4140 and 4050 s, respectively) to benefit from the full depth of the CaHK photometry is deeper than the Pan-STARRS1 data that were used to discover Tri II (Laevens et al. 2015). All were observed in service mode by the CFHT observing staff between 2015 July 18 and 2016 February 13. After pre-processing of the images with ELIXIR by CFHT (de-biasing, flat-fielding, and de-trending; Magnier & Cuillandre 2004), the images were astrometrically calibrated, stacked, and processed for photometry with the CASU pipeline (Irwin & Lewis 2001), as described in detail by Starkenburg et al. (2017). The broadband *g* and *I* photometry is calibrated on to the Pan-STARRS1 $g_{\rm P1}$ and $i_{\rm P1}$ bands and we directly use the Pan-STARRS1 photometry at the bright end, where the CFHT observations saturate. Finally, the photometric catalog is de-reddened using the Schlegel, Finkbeiner, and Davis dust maps.

Similarly to what was done for the Pristine Inner Galaxy Survey (Arentsen et al. 2020), the large number of science fibers available on Hectochelle allowed us to perform a broad selection of targets in the part of the CaHK colour–colour diagram that contains metal-poor stars. This allowed us to bypass any potential calibration issue and the use of Pan-STARRS1 broad-band magnitudes instead of the SDSS ones we relied on in Starkenburg et al. (2017). In particular, we selected stars based on their colour–magnitude diagram location so they broadly follow an old and metal-poor isochrone. In the colour–colour space using CaHK that is presented in Fig. 1 and used by the Pristine survey, we loosely select stars from the metal-poor region, using known Tri II members as a guideline to isolate other stars with similar properties. Once fibers are assigned to these high-priority stars, we fill the rest of the fibers with random colour-magnitude diagram-selected stars, irrespective of their CaHK information.

We processed all raw Hectochelle spectra using the CfA pipeline (HSRED v2.1[1]). Following the procedure described in detail by Walker, Olszewski & Mateo (2015), we then analysed each individual spectrum by fitting a model based on a library of synthetic template

[1] https://bitbucket.org/saotdc/hsred/

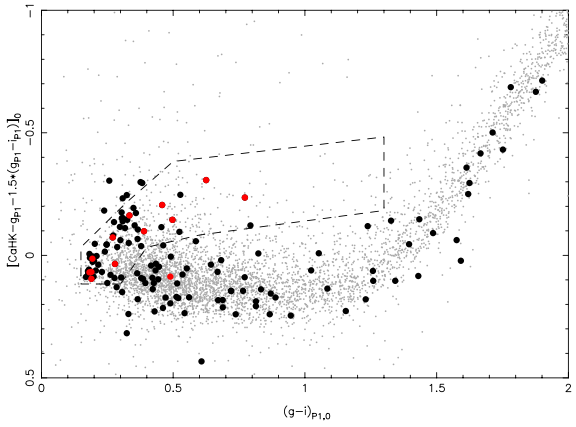

Figure 1. (CaHK, g, i) colour–colour space for Tri II. All stars in the MegaCam photometry are shown as small grey dots and follow a stellar locus that is produced by Milky Way, metal-rich stars. In this space, metal-poor stars are above this locus. Large black symbols correspond to stars within 4 arcmin of the centre of Tri II, with radial-velocity-selected, likely members shown in red. One of those stars is shown here to be metal-rich and unlikely to be a true members. Our selection for Hectoshell gives the highest priority to stars within the dashed polygon that provides a loose selection of stars away from the metal-rich foreground contamination.

spectra that span a regular grid in effective temperature, surface gravity, and [Fe/H] metallicity. In addition to the stellar-atmospheric parameters, we fit for line-of-sight velocity, as well as several free parameters that specify the continuum shape and correct for wavelength-dependent velocity shifts.

With respect to the procedure documented by Walker et al. (2015), for present purposes, we update our estimation of systematic errors associated with line-of-sight velocity and metallicity. For this task, we use our entire catalog of MMT/Hectochelle observations of dwarf galaxies and globular clusters, including observations spanning the years 2005–2020. This sample includes 12 517 independent observations of 7906 unique stars, including 2501 stars with up to 13 individual measurements. We model the pair-wise velocity and metallicity differences as a mixture of a Gaussian with an outlier model (see section 4.1 of Li et al. 2019 and section 2.2 of Pace et al. 2021). The final uncertainty ($\sigma_{v,\mathrm{calib}}$) is treated as a systematic error ($\sigma_{v,\,\mathrm{systematic}}$) plus a scaling parameter (k_v) and $\sigma^2_{v,\mathrm{calib}} = \sigma^2_{v,\,\mathrm{systematic}} + (k_v \sigma_{v,\mathrm{mcmc}})^2$. We find $k_v = 1.03 \pm 0.02$ and $\sigma_{v,\,\mathrm{systematic}} = 0.35 \pm 0.02$ km s^{-1} for the velocity systematic errors, and $k_{\mathrm{[Fe/H]}} = 1.33 \pm 0.01$ and $\sigma_{\mathrm{[Fe/H],\,systematic}} = 0.0 \pm 0.01$ for metallicity systematic errors.

2.2 Keck DEIMOS

Our sample also includes spectroscopy obtained with the Deep Extragalactic Imaging Multi-Object Spectrograph (DEIMOS; Faber et al. 2003). First, Kirby et al. (2015, 2017) observed six slitmasks in 2015 and 2016. They used the 1200G grating, which achieves a spectral resolution of $R \sim 7000$ at 8500 Å, in the spectral vicinity of the CaII infrared triplet. Secondly, Martin et al. (2016) observed two DEIMOS slitmasks with a similar spectral configuration as Kirby et al. (2015)

Kirby et al. (2015) selected stars using Keck/LRIS (Oke et al. 1995) photometry. They chose a generous selection region in the CMD around the red giant branch as defined by the ridgeline of the globular cluster M92. Martin et al. (2016) used a similar selection technique with photometry (Laevens et al. 2015) from the Large Binocular Camera. In general, the field of Tri II is sparse enough that most candidate member stars in the field of the slitmask could be observed. As a result, the samples have little selection bias due to colour (or stellar age or metallicity). Kirby et al. (2017) were mainly interested in quantifying RV variability, not in finding new members. As a result, they designed their slitmasks to target stars already identified as members by Kirby et al. (2015) and Martin et al. (2016).

Velocities were measured in slightly different ways. Kirby et al. (2015, 2017) reduced the spectra with custom modifications to the spec2d data reduction pipeline (Cooper et al. 2012). They matched empirical spectral templates observed with DEIMOS to the Tri II spectra and varied the velocity until χ^2 was minimized. Martin et al. (2016) used their own custom pipeline (Ibata et al. 2011) to reduce the spectra. They determined radial velocities from the mean wavelengths of Gaussian fits to the CaII triplet.

Slit imaging spectrographs can experience RV zero-point shifts if the star is not perfectly centred in the slit. This effect can be mitigated by observing the wavelengths of telluric absorption lines (e.g. Sohn et al. 2007). The slit centring correction is taken to be the deviation of the wavelengths of these lines from the geocentric rest frame. All of the studies used in this work performed such a correction.

2.3 Zero-point offset

In this section, we describe the calculation of the zero-point velocity offset between Keck and MMT. Although our complete set of Tri II Keck observations is a concatenation of the Kirby et al. (2017) and Martin et al. (2016) data sets, the zero-point offset between the two appears consistent with zero (see section 3.2 of Kirby et al. 2017). For this analysis, we have defined the offset as the MMT zero-point minus the Keck zero-point. There are eight objects in our data set around the Tri II galactic centre with RV measurements in both MMT and Keck catalogs. Measurements for a given object and instrument are combined into a single weighted mean value. We then calculate the offset between the sets of combined instrument velocities assuming Gaussian errors.

The methods described here and in Section 3 are based on a Gaussian likelihood function, which is described in terms of model prediction μ, model error σ, given data in the form of the observed velocity v:

$$\mathcal{G}(v|\mu,\sigma) = \frac{1}{\sqrt{2\pi(v^2_{\mathrm{error}} + \sigma^2)}} \exp\left(-\frac{(v-\mu)^2}{2(v^2_{\mathrm{error}} + \sigma^2)}\right) \quad (1)$$

This is the general likelihood for a given velocity prediction, and the total likelihood function is the product of the velocity likelihoods.

In the context of finding a zero-point offset, we apply this likelihood to a set of velocity differences $\{v_i\}$, where v_i represents the difference between the ith star's MMT weighted mean velocity and its Keck weighted mean velocity, $v_i = \bar{v}_{i,\mathrm{MMT}} - \bar{v}_{i,\mathrm{Keck}}$. We assume that these velocity differences are consistent with the zero-point offset between instruments δ_v and that there is no dispersion in δ_v, only observational errors. Thus, the total likelihood is the product of the likelihoods of individual objects, $\prod_{i=1}^{N} \mathcal{G}(v_i, \delta_v, 0)$.

However, some objects have a very large velocity difference between the instruments, possibly due to low signal to noise or unconfirmed binarity. A convenient way to account for these objects is to construct a mixture model to treat them as outliers, a similar model is used in Li et al. (2019). The new likelihood for a given object is the sum of the original Gaussian likelihood and outlier model likelihood weighted by the probability the object is an outlier.

The new likelihood is written as...

$$L(\{v_i\}|\delta_v, \gamma, p) = \prod_{i=1}^{N} [\gamma \mathcal{G}(v_i|0, p) + (1-\gamma)\mathcal{G}(v_i|\delta_v, 0)] \quad (2)$$

where γ represents the outlier fraction and δ_v represents the offset correction. The outlier model is applied to the difference in the combined weighted mean velocities for each instrument and is taken to be a Gaussian with a large standard deviation. The priors are as follows:

(i) offset δ_v: uniform(-10 km s^{-1}, 10 km s^{-1})
(ii) outlier fraction γ: uniform(0, 0.5)
(iii) outlier model standard deviation p: uniform(4 km s^{-1}, 20 km s^{-1})

We define the posterior as the Gaussian likelihood multiplied by our set of priors and look for a δ_v that maximizes this posterior. The offset error is taken as the width of this offset posterior distribution. We derive the offset value from the resulting posterior, sampled using Markov Chain Monte Carlo (MCMC) by the Metropolis–Hastings algorithm via the EMCEE PYTHON package (Foreman-Mackey et al. 2013). Applying this procedure to the eight stars in the overlapping MMT-Keck data sets observed around the Tri II galactic centre, we find an offset value of $\delta_v = -0.11 \pm 1.02$ km s^{-1}. While this value could be determined using only our Tri II data set, the large error means that the offset is not resolved within 1 km s^{-1} and the introduction of a large offset error can make it more difficult to resolve the Tri II velocity dispersion.

To improve the error on our zero-point offset between the instruments, we also include Keck/DEIMOS (Pace et al. 2020) and MMT/Hectochelle (Spencer et al. 2018) observations from an additional 288 Ursa Minor objects. The combined Tri II and Ursa Minor data set results in an offset correction of $\delta_v = -1.33 \pm 0.33$km s^{-1}.

We opt to use the offset that is calculated while including Ursa Minor observations, as the larger amount of data gives a more precise value for the offset. Thus, we bring all observations on to a common zero-point by subtracting a fixed amount of 1.33 ± 0.33 km s^{-1} from each velocity measurement obtained with Keck/DEIMOS. We do not propagate the offset error as the total error is dominated by the combination of instrument-specific systematics and random errors.

2.4 Membership

To determine Tri II membership, we sigma clip our data set at 3.5σ from both the galaxy mean line-of-sight velocity and proper motion. This step removes objects whose observations differ from the Tri II measurements >3.5 times the root sum of the squared of the galaxy and measurement errors, $\sigma = \sqrt{\sigma^2_{\text{Tri II}} + \sigma^2_{\text{obs}}}$. We use the proper motions from *Gaia* eDR3 (Gaia Collaboration 2021, Fig. 2). All members are consistent with zero parallax (i.e, $\varpi - 3\sigma_\varpi < 0$). The Tri II mean velocity is taken as -381.7 km s^{-1} (Kirby et al. 2017) and the galaxy proper motion as $\mu_{\alpha\star} = 0.58 \pm 0.06$ mas yr^{-1}, $\mu_\delta = 0.11 \pm 0.07$ mas yr^{-1} (Pace, Erkal & Li 2022). Other systemic proper motion measurements with Gaia EDR3 find similar results (McConnachie & Venn 2020; Battaglia et al. 2022). While the velocity dispersion is unresolved, we use $\sigma_{\text{Tri II}} = 4$ km s^{-1} (Fig. 3). Our resulting sample consists of 16 member stars, one of which is the previously confirmed binary star (GAIA ID 331086526201161088 which we refer to as *Star46* or MIC2016-46 in this work). There is one star that is observed by MMT only, two stars in the overlap of MMT and Keck, and the remaining 13 are observed by Keck only.

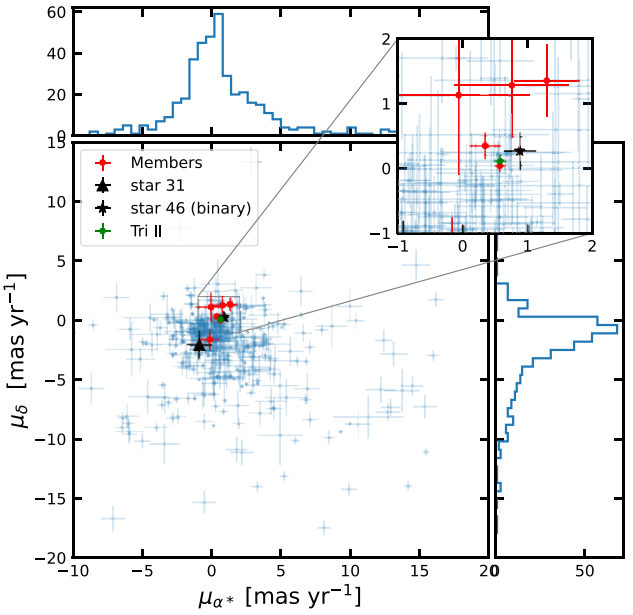

Figure 2. Proper motion distribution of stars within 10 arcmin (∼4 half-light radii) of Tri II centre from Gaia eDR3 after a parallax cut (blue). The green point marks the Tri II proper motion value that is used to determine membership. The black triangle and star are the two stars with uncertain membership in Kirby et al. (2017). The red dots are the remaining members that have Gaia proper motion measurements.

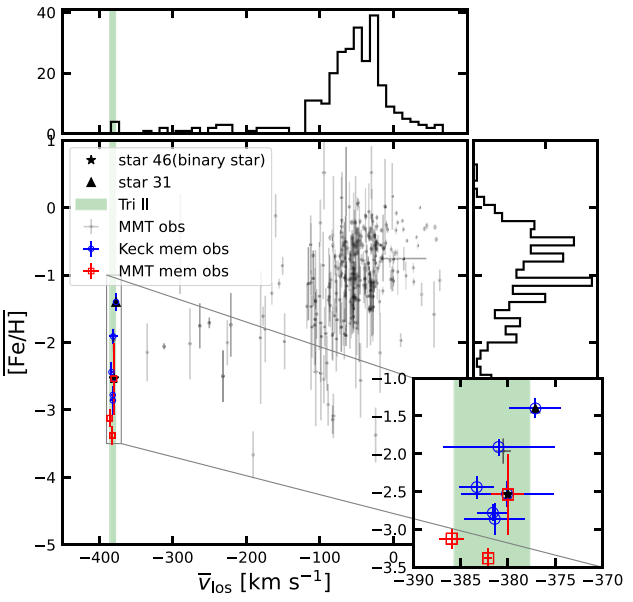

Figure 3. Mean metallicities and velocities of all stars observed in MMT around the Tri II field (black). The green area represents the Tri II mean velocity from Kirby et al. (2017) used in membership cuts. Our final sample of Tri II members is plotted with two colours/markers to distinguish between Keck (blue circles) and MMT (red squares) measurements. The binary star, alone, is plotted with the systemic velocity found in this work rather than the weighted mean of the velocity observations.

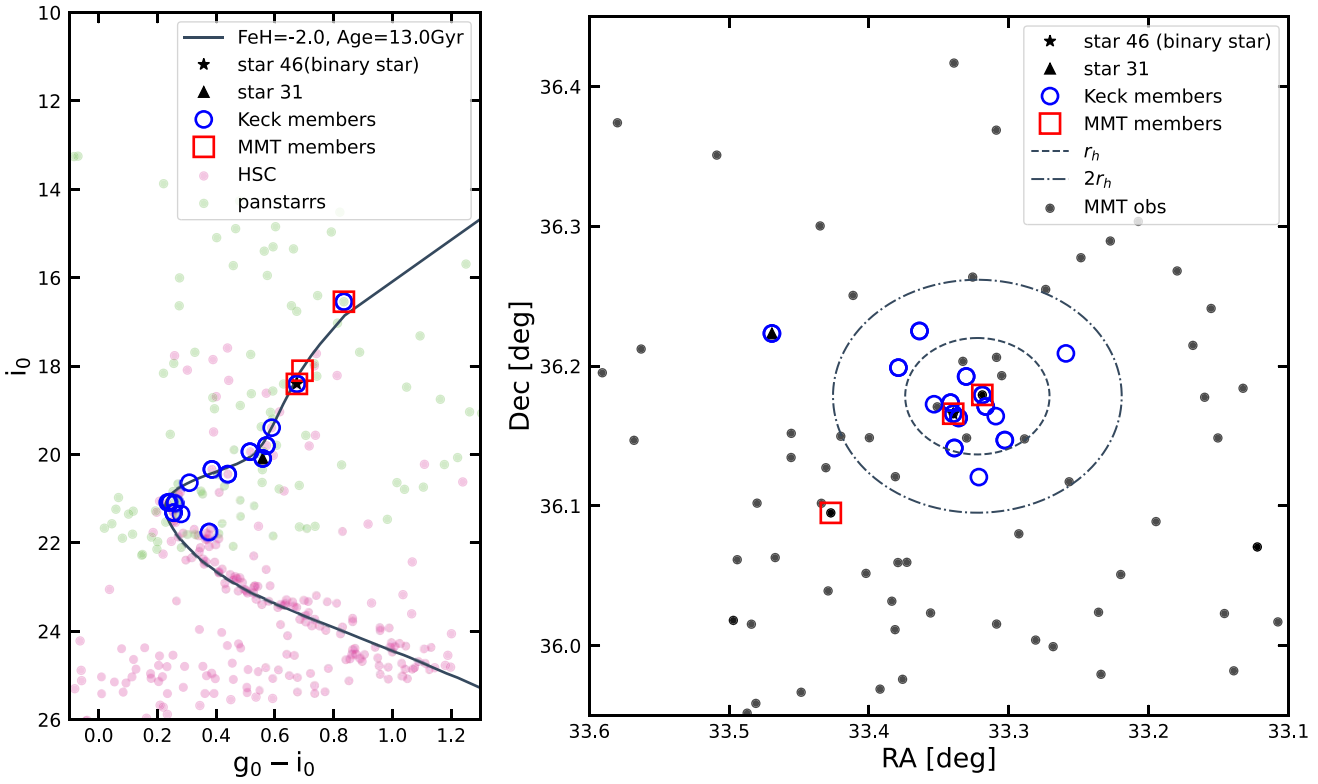

Figure 4. *Left*: colour–magnitude diagram of Tri II stars within ∼4 half-light radii (r_h =2.5 arcmin; Carlin et al. 2017) taken by HSC and Panstarrs with a MIST isochrone overlaid. The location of the Tri II binary star and *Star31* is indicated by a star and triangle, respectively. The isochrone is defined by the following values: $m - M = 17.44$, [Fe/H]=−2.2, and Age = 13 Gyr. *Right*: sky positions of members and stars observed with MMT. The dotted lines represents the 1 and 2 half-light radii of Tri II. In both plots, the members are plotted with either a red square or blue circle for MMT and Keck observations, respectively.

Fig. 4 shows the location of our final sample of member stars on a colour–magnitude diagram compared to all the stars within the Tri II half light radius after a star-galaxy separation cut observed by the Subaru/Hyper Suprime-Cam (HSC; Miyazaki et al. 2018) and Pan-STARRS1 (Flewelling et al. 2020). The isochrone parameters and the half-light radius (r_h =2.5 arcmin) are taken from Carlin et al. (2017). In Figs 2–4, we indicate the locations of the binary star (*Star46*) and another member, called *Star31* (or MIC2016-31) in this analysis, with black markers of different shapes. *Star31* is specifically marked because of its uncertainty as a member in Kirby et al. (2017; also called *Star31* in their work). Its membership is brought into question due to it being (1) far from the galactic centre, (2) the most metal-rich star in the sample (to the point of driving Tri II's [Fe/H] dispersion), and (3) the only star whose velocity is $>1\sigma$ from the galaxy mean velocity. However, the now available *Gaia* eDR3 indicate its proper motion is consistent with Tri II, bolstering its case as a member.

3 METHODS

3.1 Binary stars

When a star is a part of a binary system, the orbital motion can give rise to periodic variability in the line-of-sight velocity. If one star is much brighter than its companion (e.g. a red giant with a main-sequence companion), then a single-epoch spectrum may not show any evidence of variability. Conventional methods of combining observations, such as a weighted mean, can misrepresent the true systemic velocity if the system is sparsely observed and/or it results in an inflated error in the combined velocity. Thus, binary stars can directly inflate the calculated velocity dispersion if not accounted for properly. Though the true line-of-sight velocity will vary with time, it will oscillate around the centre-of-mass (systemic) velocity.

In terms of the true anomaly ν (angular position in the orbital plane from the periastron direction), argument of periapsis ω (angle in the orbital plane between the ascending node and the periastron) and systemic velocity v_0, a member of a binary star system has line-of-sight velocity that varies with time according to

$$V = K(\cos(\omega + \nu) + e\cos\omega) + v_0 \tag{3}$$

(Murray & Correia 2010). We can further expand the semi-amplitude K in terms of the binary parameters, period P, semimajor axis a, inclination $\sin i$, and eccentricity e as

$$K = \frac{2\pi}{P}\frac{a\sin i}{\sqrt{1-e^2}}. \tag{4}$$

This is the model that we use to fit the observed RV curves. It is worth mentioning that instead of using ν as a free parameter, we sample in Φ_0, representing the phase, which is related to a constant called *the time of periastron passage*, T, by a factor of $2\pi/P$. We can relate ν and Φ_0 using the *eccentricity anomaly*, ζ.

$$\tan\left(\frac{1}{2}\nu\right) = \sqrt{\frac{1+e}{1-e}}\tan\left(\frac{1}{2}\zeta\right) \tag{5}$$

$$\frac{2\pi}{P}(t-T) = \frac{2\pi}{P}t + \Phi_0 = \zeta - e\sin\zeta \tag{6}$$

We furthermore include a jitter parameter that acts as secondary error to account for velocity variability not due to periodic orbital

Table 1. Priors used in binary modelling and resulting orbital parameters for the Tri II binary star. The posterior is separated into short and long period solutions at the 0.6 yr (219.2 d) boundary.

	Binary star orbital parameters		
Parameter	Prior	Short Per.	Long Per.
Period P	linearly decreasing in log(P) from 1 d to 10^{10} d	$148.1^{+2.8}_{-1.4}$ d	$296.1^{+3.8}_{-3.3}$ d
Eccentricity e	Beta (1.5,1.5)	$0.29^{+0.10}_{-0.07}$	$0.50^{+0.06}_{-0.04}$
Systemic velocity v_0	Normal (0,474 km s^{-1})	$-387.6^{+0.8}_{-1.2}$ km s^{-1}	$-380.0^{+1.8}_{-1.7}$ km s^{-1}
Phase Φ_0	uniform (0,2π)	$3.12^{+2.21}_{-2.10}$	$3.25^{+2.04}_{-2.23}$
Argument of periapsis ω	uniform (0,2π)	$4.04^{+0.35}_{-0.65}$	$3.43^{+0.28}_{-0.24}$
Jitter	Normal (0 k ms^{-1}, 2 k ms^{-1})	$1.3^{+1.4}_{-0.9}$ km s^{-1}	$0.9^{+1.1}_{-0.6}$ km s^{-1}
Semimajor axis a	loguniform, bounds determined from mass	$0.71^{+0.26}_{-0.15}$ au	$1.12^{+0.41}_{-0.24}$ au
Inclination sin i	uniform (0,2π) in cos i	$0.31^{+0.08}_{-0.09}$	$0.39^{+0.11}_{-0.11}$

motion. We note that Hekker et al. (2008) found a correlation between velocity jitter and surface gravity for red-giant branch stars, where stars with $\log g \lesssim 1$ can have excess jitter ~ 1 km s^{-1}. However, the majority of our members, including *Star46*, exist on the lower red giant branch where $\log g \gtrsim 1$. This is commonly the case for stars in ultrafaint dwarfs, so there is little concern that internal mechanisms will inflate the galaxy velocity dispersion.

We continue to assume a Gaussian error on velocity measurements, thus allowing us to use the previously defined Gaussian likelihood function, equation 1. We generate samples of the posterior on the orbital binary parameters using rejection sampling. This sampling is carried out over the course of 10^5 iterations, with each iteration starting with 10^6 points before rejection. After rejection, the surviving samples across all iterations are combined. The choice to use rejection sampling instead of MCMC is due to the potential multimodality posterior. A sparsely observed binary can have multiple possible orbital period solutions, which have corresponding total mass and systemic velocity values, represented as peaks in the posterior. This specific scenario can lead to untouched areas of the posterior when using MCMC.

The priors are quite uninformative, which ensures that we can fully sample all the possible binary parameters. Note that there is a pre-defined mass range, such that the prior in total mass, is loguniform from log(0.1 $M_\odot$) to log(10 $M_\odot$), which is used to bound the semimajor axis prior. The priors on all angles are uniform. We adopt the uniform prior on cos (i) corresponding to a random orientation of binary orbits and a Beta distribution for eccentricities. The parameters for the Beta distribution are $\alpha = 1.5$ and $\beta = 1.5$, resulting in a near uniform between 0 and 1 for eccentricities, Beta(1.5, 1.5). For compactness, we explicitly state the priors on each of the orbital parameters alongside the resulting *Star46* binary parameter posteriors in Table 1.

We are able to make further assumptions about the system by modifying the surviving posterior samples. We remove non-physical solutions corresponding to close binaries where the pericenter is less than the stellar radius or where the mass of the companion star is negative. These stellar radii and masses are calculated using the *Isochrones* PYTHON package (Morton 2015) to determine stellar parameters for the binary star of age 13 Gyr, [Fe/H] of -2.2, and distance modulus of 17.24 using the MESA Isochrones and Stellar Tracks (MIST) grid (Dotter 2016; Choi et al. 2016). Fig. 4 shows the relevant isochrone fit on a colour–magnitude diagram with Tri II members plotted. For the binary star *Star46*, we determine a mass of $M_{\rm bin} = 0.777$ $M_\odot$ and stellar radius of $r_{\rm bin} = 0.027$ au from an isochrone fit to Tri II stars. We equivalently derive a mass and radius for the other Tri II members by finding the point on the isochrone closest to each member star using the same steps.

Similarly, Raghavan et al. (2010) looked at 259 confirmed solar-type binaries in the *Hipparcos* catalog and found that the periods are distributed according to a lognormal distribution with $\mu_{\log P} = 5.03$ and standard deviation $\sigma_{\log P} = 2.28$, where P is in days. This is a more informative prior on the period than our default period prior. We refer to this lognormal distribution as the 'Raghavan prior' for the remainder of this paper. We present this distribution with the minor caveat that most of the detectable member stars of dwarf galaxies are not solar-type (main-sequence) stars, but rather red giant branch stars.

We are able to infer the posterior under this prior by re-sampling from the current surviving samples with non-uniform weights. These weights are proportional to the ratio of the Raghavan period distribution to the default prior. All of these assumptions shift the posterior away from shorter orbital periods, but as we will see in Section 4.2, the application of this prior on *Star46* significantly alters the parameter posterior. As such, we present the results both before and after the application of the Raghavan prior.

3.2 Non-binary stars

In the case of non-binary stars, we expect line-of-sight velocity observations to be consistent with a constant velocity model with some scatter in each measurement proportional to the observational error. Our goal is to determine a star's true velocity by combining multiple epochs of RV measurements into one stellar velocity. A common approach to this is calculating the weighted mean – i.e. summing the measurements weighted by the inverse of the squared errors. This approach has the benefits of being analytic and thus not computationally intensive. However, it has the downside of underestimating the error when dealing with potentially variable systems. In this section, we offer another method to calculate the true stellar velocity by finding its posterior distribution.

Once again, the assumption of Gaussian error allows us to use the previously defined Gaussian likelihood function, equation 1, and a set of priors in true velocity and velocity error to sample from the true velocity posterior. The sampling is done using MCMC sampling and is performed with 24 walkers, 1000 steps each, and 100 step burn-in. For a set of line-of-sight velocity observations $\{v_i\}$ with errors $\{\epsilon_i\}$, we define a uniform prior in true velocity that is non-zero from min ($\{v_i\}$) $-$ 4max ($\{\epsilon_i\}$) to max ($\{v_i\}$) + 4max ($\{\epsilon_i\}$). We also use Jeffrey's prior for the standard deviation of a Gaussian distribution ($1/\sigma$ or uniform in log σ) for the true velocity error. The error of the combined velocity measurement is taken as one

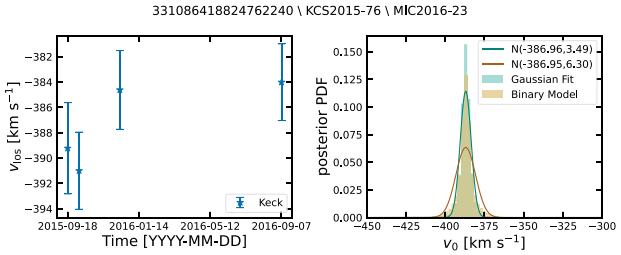

Figure 5. *Left:* RV curve of *Star 23*, a Tri II member with more than one observation. The velocity measurements are coloured by instrument with the same labeling as Fig. 6. *Right:* corresponding posterior on the mean velocity resulting from both the Gaussian fit and binary model. The binary model posterior samples have had both modifications that remove short period solutions to reduce the posterior scatter.

standard deviation from the posterior on the mean. We use the mixture sub package found in *scikit-learn* (Pedregosa et al. 2011) to fit a Gaussian mixture model (GMM) of a singular Gaussian to the resulting posterior samples. Fig. 5 shows the RV curve and resulting posteriors using this method, referred to as the Gaussian fit method, and binary model method for an example Tri II member star with multiple velocity observations.

This Gaussian Fit method has the advantage in that it does not assume binarity but does retain increased error with larger variability in the RV curve, more than the weighted mean. For comparison, we also calculate the combined velocities under the weighted mean and binary model methods (Fig. 6). Applying the binary model to the assumed non-binary member stars takes up significantly more computation time and results in a larger uncertainty in the combined velocity. Over short time-scales, the observations can be consistent with either a constant velocity model or the RV curve of a long period binary. These methods are only applied to members with more than one velocity measurement as neither would be informative for stars with only a single epoch. Using the Gaussian Fit method would be the equivalent of trying to fit a Gaussian distribution to a single point. For the binary model, there is not enough information in a single epoch to restrict the possible binary solutions.

3.3 Mean velocity and velocity dispersion

The Tri II velocity dispersion can be inferred from the posterior using the same Gaussian likelihood function as in previous sections (equation 1). We define another Gaussian model in terms of the mean velocity $\bar{v}$ and the velocity dispersion σ_v of the galaxy. The total likelihood is the product of the likelihood of the model on the stellar velocity of each member. For stars with multiple velocity measurements, the measured velocities are combined using one of the methods presented in the previous sections. In the case of a multimodal posterior, such as for *Star46*, we must fit a 1D GMM to the systemic velocity posterior and the likelihood for that object becomes

$$L = \sum_{j}^{n} w_j \mathcal{G}(\mu_j | \bar{v}, \sigma_v) \tag{7}$$

where μ_j and w_j represent the mean and weight of the jth Gaussian in the mixture model with n Gaussians. The error on μ_j is taken as the standard deviation of the Gaussian σ_j and the number of Gaussians in the GMM is determined by manually inspecting the v_0 posterior. Fig. 7 shows the GMM fits to the *Star46* systemic velocity posterior before and after the application of the Raghavan prior.

The velocity dispersion prior is log-uniform from $\log_{10}(0.05$ km s$^{-1})$ to $\log_{10}(100$ km s$^{-1})$, which is equivalent to Jeffrey's prior. The minimum value corresponds to the case where the galactic dynamics are fully determined by visible matter (see Appendix A). We have chosen to find the posterior of $\log_{10}\sigma_v$ rather than σ_v to better sample smaller velocity dispersion values. Once again, we use a uniform prior from $\min(\{v_i\}) - 4\max(\{\epsilon_i\})$ to $\max(\{v_i\}) + 4\max(\{\epsilon_i\})$ as our prior on mean velocity.

4 RESULTS

4.1 Binary orbital parameters

Within our data set, we are able to spectroscopically identify one star, *Star46*, as a binary. Attempting to fit a constant velocity model to the observations of this object, we find a reduced chi-squared of $\chi_{\rm red} = 157.2$. Previous analyses by Venn et al. (2017) and Kirby et al. (2017) found this star to be a part of a binary system. For comparison, the member with the second-highest reduced chi-squared is MIC2016-27 with $\chi_{\rm red} = 4.4$. Although this value could suggest possible binarity for MIC2016-27, its velocity variations are more consistent with a constant-velocity model than *Star46*.

In this analysis, we use the four velocity measurements of this star from MMT (Table D1) and five from Keck (Table D2). There are two additional velocity measurements made in Geminin/GRACES data (Venn et al. 2017; Ji et al. 2020) that we have opted to not use for two reasons. First, the inclusion of this data would add an additional unknown zero-point correction that is more difficult to quantify due to less overlap in number of stars. Secondly, we have explored, including them, and found that they do not impact the resulting orbital parameter posterior (see Appendix B).

After an initial pass with our model on *Star46*, we find that there are two noticeable peaks in the posterior corresponding to periods of ∼0.4 and ∼0.8 yr. We are able to eliminate the sub-harmonics (e.g. 0.2, 0.1 yr) from our restrictions on pericenter and Kepler's third law both limiting the allowed semimajor axis values. Because the period modes are distinct, we re-run the sampling with a more restricted period prior bound at 0.3 and 0.95 yr to ensure a larger number of surviving posterior samples. The resulting binary orbital parameters presented in this section are derived from the posterior after removing samples that correspond to a negative companion mass but before the application of the Raghavan prior. Fig. 8 is a corner plot of the posterior of select parameters and shows two distinct peaks corresponding to long and short period solutions. We separate the posterior samples at the 0.6 yr boundary and present the orbital parameter values taken from the truncated posteriors in Table 1. Fig. 9 shows the RV curve for this star, as well as the orbital solutions that correspond to the surviving samples.

The posteriors of the semimajor axis for both solutions are consistent with values less than $a = 2$au, indicating that this is a close binary. The resulting overall binary parameter space is that of a common binary star system. The companion mass posterior is not distinct enough from the prior to be informative, but all of the samples correspond to stellar masses potentially on the main sequence.

For comparison, the only other binary star in an ultrafaint dwarf spheroidal, Her-3 in the Hercules dwarf, has a smaller eccentricity ($e_{\rm Her\text{-}3} = 0.18$) and period ($P_{\rm Her-3} = 135.28 \pm 0.33$d) values (Koch et al. 2014). Plugging into equation 4, we find the corresponding semi-amplitudes, $K_{\rm short} = 16.24^{+1.59}_{-1.17}$ km s^{-1} and $K_{\rm long} = 18.72^{+2.67}_{-1.59}$ km s^{-1}, which are only slightly larger than Herc-3's solution, $K_{\rm Her-3} = 14.48 \pm 0.82$ km s^{-1}.

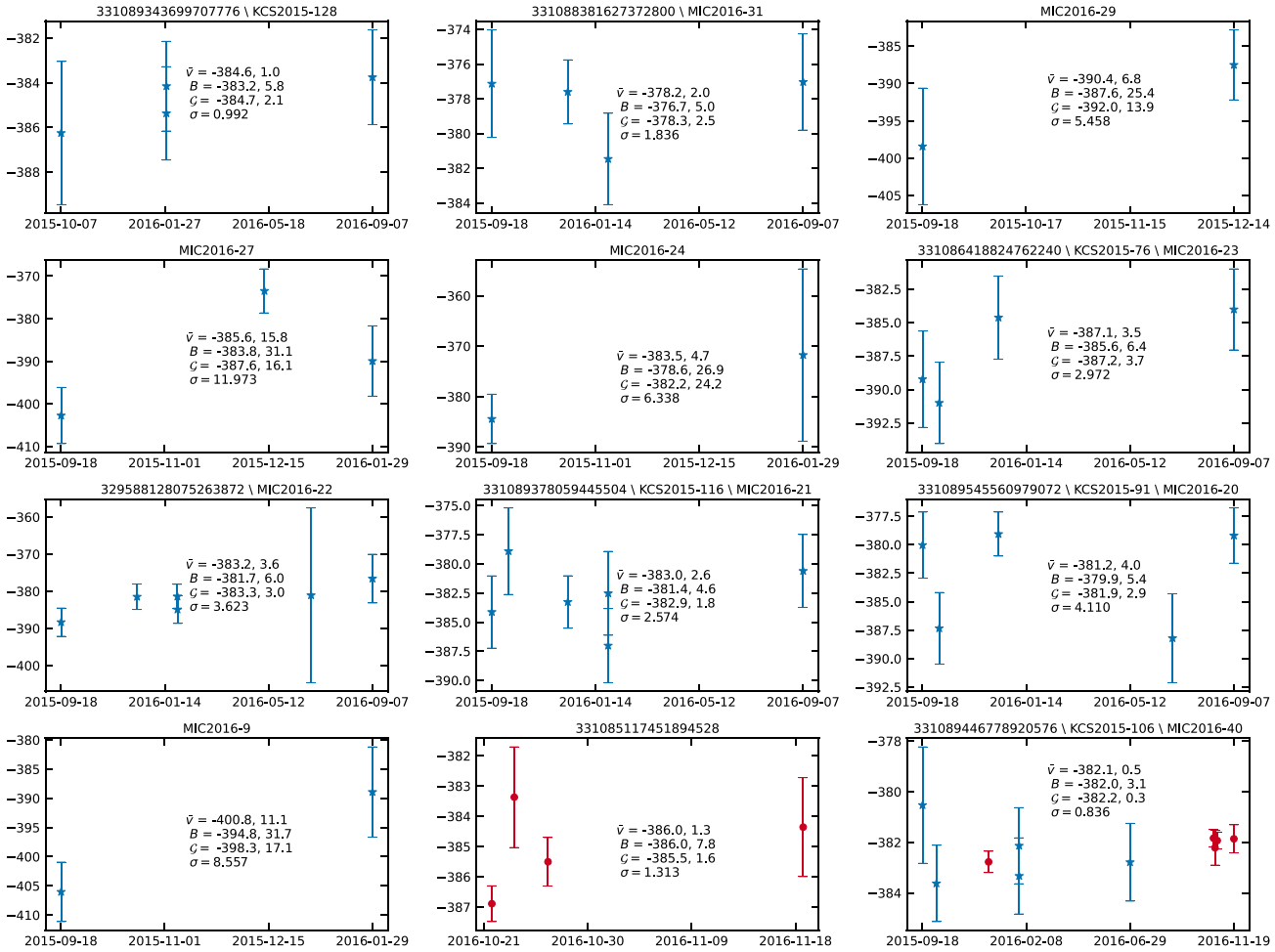

Figure 6. RV curves of the 12 non-binary member stars with multiple epochs. The different values are the results of different methods of combining observations. $\bar{v}$: weighted mean; B: fitting a Gaussian distribution to the binary model v_0 posterior; $\mathcal{G}$: assuming the observations are taken from a Gaussian distribution centred on a true systemic velocity. For comparison, the standard deviation of the observations is also listed (σ). The stars are identified by their Gaia ID when applicable. All values listed and on the y-axis are in km s^{-1}. The dates are in the format year-month-day.

The truncation in companion mass slightly shifts the posterior towards longer periods, but not more than 0.2 km s^{-1}, much smaller than the width of the posterior peaks (~ 2 km s^{-1}). Reweighting the samples so that the prior is the Raghavan period distribution weights the posterior in favour of the longer period solutions and the corresponding larger systemic velocities, removing the multimodality of the posterior (Fig. 7). Even before applying the Raghavan prior, there is a strong preference towards the long period solutions as the ratio of the long period posterior to short period posterior is approximately 5:2. After applying the Raghavan prior, the posterior becomes almost entirely in favour of the long period solution as the ratio becomes 80:1, effectively removing the short period mode. As such, we present the parameters corresponding to the long period mode as the orbital solution, but we also explore the effect using the Raghavan prior has on the velocity dispersion.

This binary star is only 1 of the 16 stars in our sample. Moe, Kratter & Badenes (2019) and Mazzola et al. (2020) found that the intrinsic close binary fraction is anticorrelated with metallicity such that Tri II's metallicity value of [Fe/H] $= -2.1$ implies a close binary fraction $f_{\rm bin,close} \approx 0.5$. This suggests that there are more close binary members, but the current data are not enough to determine binarity for any other binaries in the galaxy. Though, with growing observation power, they may one day be observed sufficiently.

4.2 Triangulum II dynamics

While we have briefly explored applying the binary model to the non-binary members and applying the Gaussian fit model to *Star46*, we unsurprisingly find that the best variation is to treat confirmed the binary star under the binary model and the remaining members under the Gaussian fit model. This option assumes variability for only *Star46*. These additional variations made it more difficult to resolve the dispersion and instead resulted in a posterior with a maximum at the σ_v prior's minimum value. Thus, we focus our final results on the best variation.

The galaxy mean velocity posterior is consistent with the previously found mean velocity of Tri II, $\langle v \rangle = -381.7 \pm 1.1$ km s^{-1} (Kirby et al. 2017) within 2σ, where σ is the error on the mean velocity from the posterior. We present a mean velocity of $\langle v \rangle = -382.3 \pm 0.7$ km s^{-1} from this analysis. However, even in this best variation, we were unable to completely resolve the velocity dispersion.

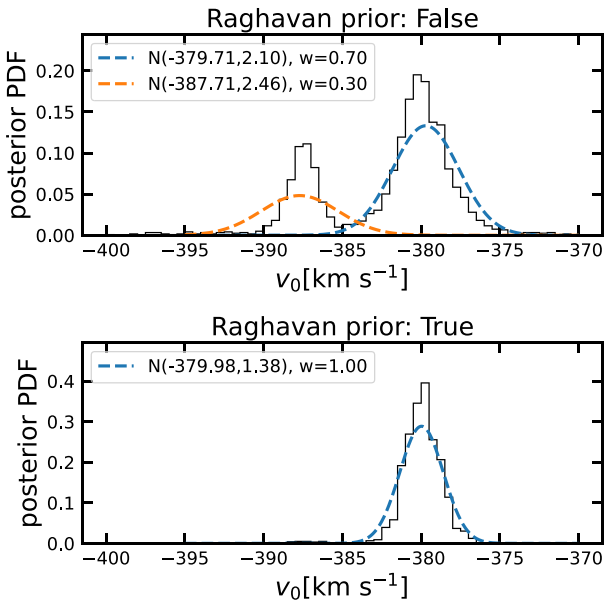

Figure 7. The posterior on the systemic velocity of the binary star and the GMM fit under different conditions. These conditions are a re-weight of the samples such that the period prior is the Raghavan distribution and removing non-physical samples.

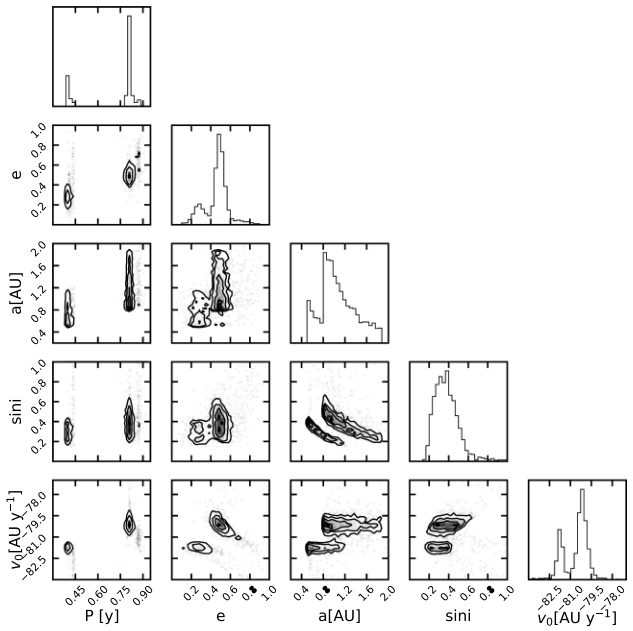

Figure 8. Orbital parameters' posterior for the binary star derived from our binary model. There are two distinct modes corresponding to.

The posterior has a small peak at $\log_{10}\sigma_v = 0.2$ (which corresponds to $\sigma_v = 1.6$km s^{-1}), but a large probability tail that stretches back to the minimum value. We see that applying the Raghavan prior only slightly reduces this tail (Fig. 10). Fig. 11 shows the complete posterior with the binary under the Raghavan prior. This remaining tail of probability means we were unable to resolve the velocity dispersion of Tri II, and we instead present upper limits

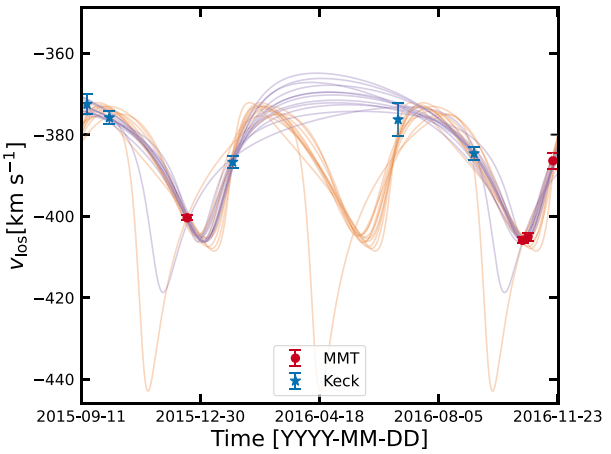

Figure 9. Possible fits to the RV curve of the binary star, *Star46*, calculated using our binary model. The orange and purple lines correspond to solutions with orbital periods of approximately 0.4 and 0.8 yr, respectively. The dates are in the format year-month-day.

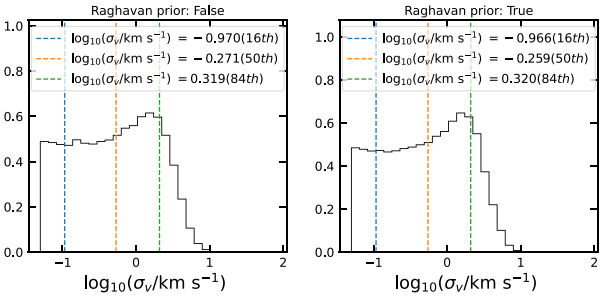

Figure 10. Velocity dispersion posterior with and without the use of the Raghavan prior on *Star46*. The 16th, 50th, and 84th percentiles are marked by the blue, orange, and green lines, respectively.

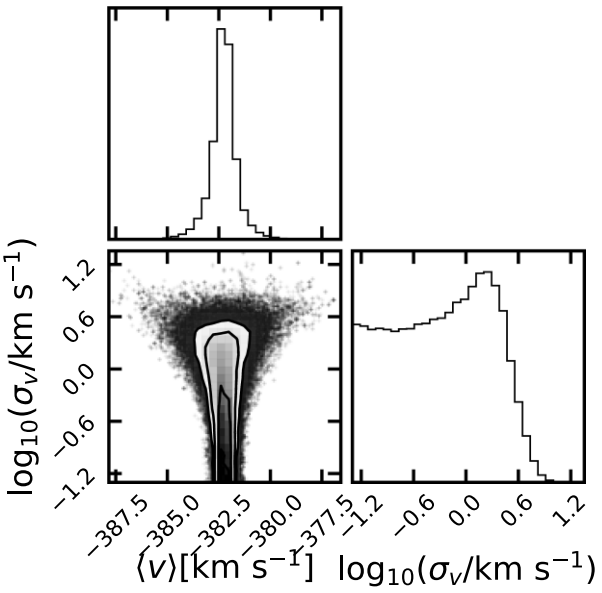

Figure 11. Complete posterior Tri II mean velocity and velocity dispersion when treating the binary star under the binary model and other non-binary members under the Gaussian fit with the Raghavan prior.

on σ_v. Before applying the Raghavan prior, we find a 90 per cent confidence limit of 2.7 km s^{-1} and 95 per cent confidence limit of 3.5 km s^{-1}. After applying the Raghavan prior, we find a 90 per cent confidence limit of 2.6 km s^{-1} and 95 per cent confidence limit of 3.4 km s^{-1}. Due to the differences between these values being so small, we again choose to present the values determined using the more informative period prior.

5 CONCLUSIONS

We have found orbital parameters for the Tri II binary star member, *Star46*. This is now the second binary star within an ultrafaint dwarf with an orbital solution after Her-3 in Hercules Dwarf (Koch et al. 2014). In doing so, we have demonstrated a method of accounting for binary star systems in velocity dispersion calculations that does not demand the removal of such systems. We also see that using our binary model when unnecessary, such as with non-binary stars, not only adds lengthy computation time, but can lead to an overestimation of velocity error.

The classification of Tri II as either an ultrafaint dwarf or globular cluster remains an open question. Though the use of this model has offered an improved analysis of the dwarf galaxy, we were unable to resolve a velocity dispersion that would confirm the existence of a dark matter halo in Tri II. However, Kirby et al. (2017) found a metallicity dispersion of $\sigma([\mathrm{Fe/H}] = 0.53^{+0.38}_{-0.12}$dex when including all available metallicity measurements for the data set. They make clear that metallicity dispersion relied on the membership two stars, *Star31* and *Star46*, despite knowing that *Star46* is in a binary system. The *Gaia* proper motions of both stars confirm that they are Tri II members [Fig. 2; also see McConnachie & Venn 2020, and Pace, (in preparation)]. We briefly tested performing the same $\sigma([\mathrm{Fe/H}])$ calculation while including the new MMT metallicities. We found that the inclusion of MMT measurements did not significantly impact the resulting dispersion where the difference after inclusion was $\lesssim 0.03$ dex from the previous value (see Appendix C). This metallicity dispersion greatly strengthens the case for Tri II's classification as a dwarf galaxy, indicating the system is embedded in a dark matter halo (Willman & Strader 2012).

The choice to apply our binary model to only one star means that we are operating with a hard binary fraction of $f_{\mathrm{bin}} \approx 0.06$. A more informed model would be to assume that there is some non-zero fraction of the 'non-binary' member stars that are actually binaries. Each star would have an associated binary and non-binary likelihoods that are calculated from marginalizing over the binary parameter posterior. These likelihoods would allow for the sampling of binary fraction as a parameter alongside with mean velocity and velocity dispersion, forming a hierarchical model that builds from the set of binary posteriors. This likelihood would be functionally similar to the mixture model used to determine the offset between the instrumental zero-point velocities. However, this approach introduces complications, as marginalization becomes less straightforward when modifying the posterior. For instance, removing binary samples based on a parameter, such as pericenter, makes the posterior no longer normalized to the calculated binary/non-binary likelihoods. The likelihoods must be re-normalized after truncation for every additional condition that is imposed. Though it is outside the scope of this paper, we find the hierarchical model to be an interesting problem and important step to explore in future works.

ACKNOWLEDGEMENTS

This work is supported in part by National Science Foundation (NSF) grants AST-1813881 and AST-1909584. ENK is supported by NSF grant AST-1847909, and he gratefully acknowledges support from a Cottrell Scholar award administered by the Research Corporation for Science Advancement. EO is partially supported by NSF grant AST-1815767. NC is supported by NSF grant AST-1812461. MM is supported by U.S. NSF grants AST-1312997, AST-1726457 and AST-1815403. ES acknowledges funding through VIDI grant 'Pushing Galactic Archaeology to its limits' (with project number VI.Vidi.193.093), which is funded by the Dutch Research Council (NWO). CB and CMD are supported by NSF grant AST-1909022.

This work has made use of data from the European Space Agency (ESA) mission *Gaia* (https://www.cosmos.esa.int/gaia), processed by the *Gaia* Data Processing and Analysis Consortium (DPAC; https://www.cosmos.esa.int/web/gaia/dpac/consortium). Funding for the DPAC has been provided by national institutions, in particular the institutions participating in the *Gaia* Multilateral Agreement.

The Pan-STARRS1 Surveys (PS1) and the PS1 public science archive have been made possible through contributions by the Institute for Astronomy, the University of Hawaii, the Pan-STARRS Project Office, the Max-Planck Society and its participating institutes, the Max Planck Institute for Astronomy, Heidelberg and the Max Planck Institute for Extraterrestrial Physics, Garching, The Johns Hopkins University, Durham University, the University of Edinburgh, the Queen's University Belfast, the Harvard-Smithsonian Center for Astrophysics, the Las Cumbres Observatory Global Telescope Network Incorporated, the National Central University of Taiwan, the Space Telescope Science Institute, the National Aeronautics and Space Administration under Grant No. NNX08AR22G issued through the Planetary Science Division of the NASA Science Mission Directorate, the National Science Foundation Grant No. AST-1238877, the University of Maryland, Eotvos Lorand University (ELTE), the Los Alamos National Laboratory, and the Gordon and Betty Moore Foundation.

This research has made use of NASA's Astrophysics Data System Bibliographic Services. This paper made use of the Whole Sky Database (wsdb) created by Sergey Koposov and maintained at the Institute of Astronomy, Cambridge by Sergey Koposov, Vasily Belokurov, and Wyn Evans with financial support from the Science & Technology Facilities Council (STFC) and the European Research Council (ERC).

Observations reported here were obtained at the MMT Observatory, a joint facility of the University of Arizona and the Smithsonian Institution. The authors wish to recognize and acknowledge the very significant cultural role and reverence that the summit of Maunakea has always had within the indigenous Hawaiian community. We are most fortunate to have the opportunity to conduct observations from this mountain.

New observations reported here were obtained at the MMT Observatory, a joint facility of the Smithsonian Institution and the University of Arizona. Some of the data presented herein were obtained at the W. M. Keck Observatory, which is operated as a scientific partnership among the California Institute of Technology, the University of California, and the National Aeronautics and Space Administration. The Observatory was made possible by the generous financial support of the W. M. Keck Foundation.

DATA AVAILABILITY

The processed MMT/Hectochelle catalog for Tri II targets are publicly available at the Zenodo database, https://doi.org/10.5281/zenodo.6561483.

REFERENCES

Arentsen A. et al., 2020, MNRAS, 496, 4964
Badenes C. et al., 2018, ApJ, 854, 147
Battaglia G., Taibi S., Thomas G. F., Fritz T. K., 2022, A&A, 657, A54
Bullock J. S., Boylan-Kolchin M., 2017, ARA&A, 55, 343
Carlin J. L. et al., 2017, AJ, 154, 267
Choi J., Dotter A., Conroy C., Cantiello M., Paxton B., Johnson B. D., 2016, ApJ, 823, 102
Cooper M. C., Newman J. A., Davis M., Finkbeiner D. P., Gerke B. F., 2012, Astrophysics Source Code Library, record ascl:1203.003
Dotter A., 2016, ApJS, 222, 8
Errani R., Peñarrubia J., Walker M. G., 2018, MNRAS, 481, 5073
Faber S. M. et al., 2003, in Iye M., Moorwood A. F. M., eds, SPIE Conf. Ser., Vol. 4841, Instrument Design and Performance for Optical/Infrared Ground-based Telescopes. SPIE, Bellingham, p. 1657
Flewelling H. A. et al., 2020, ApJS, 251, 7
Foreman-Mackey D., Hogg D. W., Lang D., Goodman J., 2013, PASP, 125, 306
Gaia Collaboration, 2021, A&A, 649, A1
Hekker S., Snellen I. A. G., Aerts C., Quirrenbach A., Reffert S., Mitchell D. S., 2008, Journal of Physics: Conference Series, 118, 012058
Ibata R., Sollima A., Nipoti C., Bellazzini M., Chapman S. C., Dalessandro E., 2011, ApJ, 738, 186
Illingworth G., 1976, ApJ, 204, 73
Irwin M., Lewis J., 2001, New Astron. Rev., 45, 105
Ji A. P., Simon J. D., Frebel A., Venn K. A., Hansen T. T., 2019, ApJ, 870, 83
Kirby E. N., Cohen J. G., Simon J. D., Guhathakurta P., 2015, ApJ, 814, L7
Kirby E. N., Cohen J. G., Simon J. D., Guhathakurta P., Thygesen A. O., Duggan G. E., 2017, ApJ, 838, 83
Koch A., Hansen T., Feltzing S., Wilkinson M. I., 2014, ApJ, 780, 91
Koposov S. E. et al., 2011, ApJ, 736, 146
Laevens B. P. M. et al., 2015, ApJ, 802, L18
Li T. S. et al., 2019, MNRAS, 490, 3508
Magnier E. A., Cuillandre J. C., 2004, PASP, 116, 449
Martin N. F. et al., 2016, ApJ, 818, 40
Martinez G. D., Minor Q. E., Bullock J., Kaplinghat M., Simon J. D., Geha M., 2011, ApJ, 738, 55
Mateo M. L., 1998, ARA&A, 36, 435
Mazzola C. N. et al., 2020, MNRAS, 499, 1607
McConnachie A. W., 2012, AJ, 144, 4
McConnachie A. W., Côté P., 2010, ApJ, 722, L209
McConnachie A. W., Venn K. A., 2020, Research Notes of the AAS, 4, 229
Minor Q. E., 2013, ApJ, 779, 116
Minor Q. E., Martinez G., Bullock J., Kaplinghat M., Trainor R., 2010, ApJ, 721, 1142
Minor Q. E., Pace A. B., Marshall J. L., Strigari L. E., 2019, MNRAS, 487, 2961
Miyazaki S. et al., 2018, PASJ, 70, S1
Moe M., Kratter K. M., Badenes C., 2019, ApJ, 875, 61
Morton T. D., 2015, Astrophysics Source Code Library, record ascl:1503.010
Murray C. D., Correia A. C. M., 2010, in Seager S., ed., Keplerian Orbits and Dynamics of Exoplanets. University of Arizona Press, Tucson, AZ, p. 15
Oke J. B. et al., 1995, PASP, 107, 375
Olszewski E. W., Pryor C., Armandroff T. E., 1996, AJ, 111, 750
Pace A. B. et al., 2021, ApJ, 923, 77
Pace A. B. et al., 2020, MNRAS, 495, 3022
Pace A. B., Erkal D., Li T. S., 2022, preprint (arXiv:2205.05699)
Pedregosa F. et al., 2011, J. Mach. Learn. Res., 12, 2825
Price-Whelan A. M., Hogg D. W., Foreman-Mackey D., Rix H.-W., 2017, ApJ, 837, 20
Raghavan D. et al., 2010, ApJS, 190, 1
Simon J. D., 2019, ARA&A, 57, 375
Sohn S. T. et al., 2007, ApJ, 663, 960
Spencer M. E., Mateo M., Walker M. G., Olszewski E. W., McConnachie A. W., Kirby E. N., Koch A., 2017, AJ, 153, 254
Spencer M. E., Mateo M., Olszewski E. W., Walker M. G., McConnachie A. W., Kirby E. N., 2018, AJ, 156, 257
Starkenburg E. et al., 2017, MNRAS, 471, 2587
Szentgyorgyi A. et al., 2011, PASP, 123, 1188
Tolstoy E., Hill V., Tosi M., 2009, ARA&A, 47, 371
Venn K. A., Starkenburg E., Malo L., Martin N., Laevens B. P. M., 2017, MNRAS, 466, 3741
Walker M. G., Mateo M., Olszewski E. W., Peñarrubia J., Evans N. W., Gilmore G., 2009, ApJ, 704, 1274
Walker M. G., Olszewski E. W., Mateo M., 2015, MNRAS, 448, 2717
Willman B., Strader J., 2012, AJ, 144, 76
Wolf J., Martinez G. D., Bullock J. S., Kaplinghat M., Geha M., Muñoz R. R., Simon J. D., Avedo F. F., 2010, MNRAS, 406, 1220

APPENDIX A: LOWER LIMIT ON $\log_{10}\sigma_v$ PRIOR

From the virial theorem, we know that the mass contained within the half-light radius of a dwarf galaxy in virial equilibrium can be described by

$$M(< R_{1/2}) = C\frac{R_{1/2}\sigma_v^2}{G} \tag{A1}$$

where σ_v is the galaxy's velocity dispersion, G is the gravitational constant, and C is a proportionality constant. Assuming that all of the mass is accounted for by the total stellar mass, the following relation becomes true.

$$M(< R_{1/2}) = \frac{\Upsilon L}{2} \tag{A2}$$

where Υ is the stellar mass-to-light ratio and L is the total luminosity. Combining these, we can solve for σ_v.

$$\sigma_v = \sqrt{\frac{G}{2C}\frac{\Upsilon L}{R_{1/2}}} \tag{A3}$$

It is estimated that Tri II has a total luminosity $L \sim 400\ \mathrm{L}_\odot$ and a half-light radius $R_{1/2} \sim 34$ pc (Laevens et al. 2015). Stellar mass-to-light ratios usually exist in the rage $\Upsilon \sim 0.5$ to $3.0\ \mathrm{M}_\odot\ \mathrm{L}_\odot^{-1}$ and the proportionality constant is in the range $C \sim 2$–4. Taking the lower limit for Υ and the upper limit for C, we find that σ_v can go as small as $0.05\ \mathrm{km\ s^{-1}}$. This value will serve as the lower limit of our velocity dispersion prior and corresponds to a system where the dynamics are fully determined by visible matter.

APPENDIX B: GRACES

We briefly explored how the inclusion of the *Star46* measurements in Venn et al. (2017) and Ji et al. (2020) would impact the binary orbital parameter posterior. For this, we do not apply an offset to the velocities measured in GRACES because of the lack of overlap in observation fields between GRACES and either MMT or Keck. Fig. B1 shows the new epochs relative to the RV curve presented in the main text (see Table B1 for the individual epoch measurements).

The spectra taken in 2015 December are reduced using different pipelines in the two papers, resulting in slightly different but consistent measured velocities for the same epoch (see section 2 of Venn et al. 2017 and section 2 of Ji et al. 2020).

Table B1. Additional GRACES observations of the Tri II binary, *Star46*.

Source	HJD	v_{los} (km s^{-1})
Venn et al. 2017	2457372.5	-397.1 ± 2.0
Ji et al. 2020	2457372.5	-396.5 ± 3.2
Ji et al. 2020	2457638.5	-381.5 ± 5.0

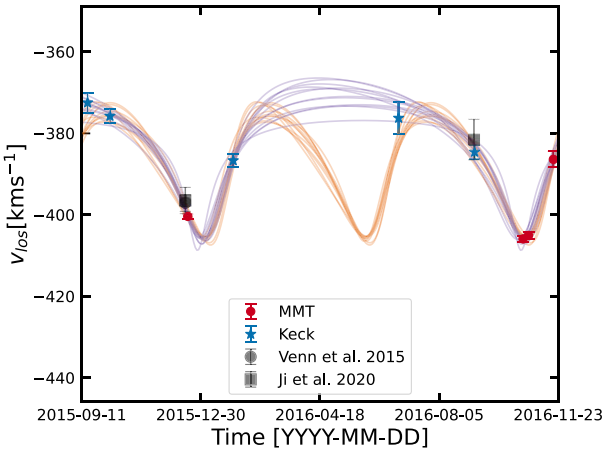

Figure B1. RV curve of *Star46*, including GRACES epochs. The Venn et al. (2017) epoch and the first Ji et al. (2020) epoch overlap. The orbital solutions plotted are the results of finding orbital solutions to the inclusion of the two Ji et al. (2020) observations. The orange and purple lines correspond to solutions with orbital periods of approximately 0.4 and 0.8 yr, respectively.

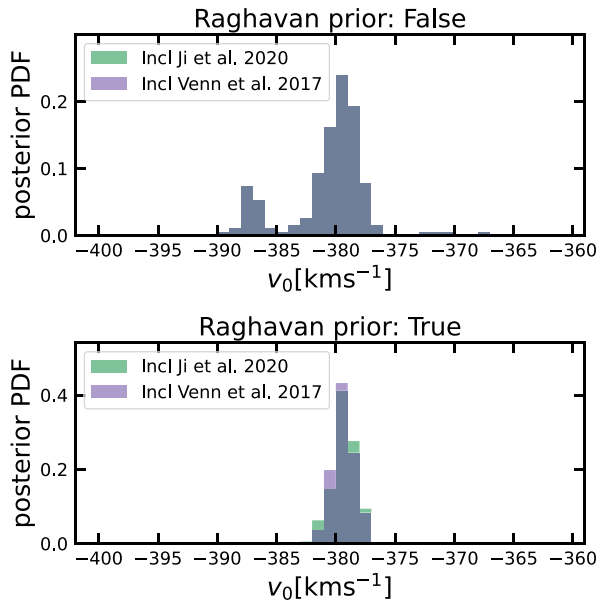

Figure B2. Resulting systemic velocity posteriors for *Star46* when including GRACES epochs. The posteriors from including Venn et al. (2017) and Ji et al. (2020) are over plotted in different colours. The overlap in the histograms is coloured grey.

Fig. B2 shows the inferred systemic velocity posterior when including GRACES observations. Under the default period prior, the posterior takes on the same bimodal shape as seen in Section 4.1 regardless of which set of GRACES observations is used. Compared to the posteriors of the systemic velocity found in the main text, with modes at $-387.6^{+0.8}_{-1.2}$ km s^{-1} and $-380.0^{+1.8}_{-1.7}$ km s^{-1}, there is a slight shift in the long-period systemic velocity. The new corresponding modes are at $-387.18\pm^{0.81}_{0.69}$ km s^{-1} and $-379.51\pm^{1.32}_{1.51}$ km s^{-1} when including either set of GRACES observations. Applying the period distribution found in Raghavan et al. (2010), there is again re-weighting towards the long-period solutions. There is a very small disparity between the resulting unimodal posteriors with the systemic velocity, becoming $-379.48\pm^{1.14}_{0.87}$ when using Ji et al. (2020)'s observations and $-379.38\pm^{0.98}_{1.22}$ when using Venn et al. (2017)'s observation. However, the differences of these posteriors from those in the main text are well within error.

While these new values have slightly smaller errors, this improvement may likely vanish after properly accounting for any zero-point offsets between GRACES and MMT or Keck. This is also not a clear conclusion of which of the two GRACES sets is preferable for this analysis. Rather than exploring this avenue that would likely yield only a marginal improvement, we opt to not include the GRACES observations of this star in this paper.

APPENDIX C: METALLICITY DISPERSION

In this section, we briefly explore how the addition of the new MMT data affects the metalicity disperison of Tri II. From repeat measurements in the MMT catalog, we only consider measurements with an Fe/H error < 0.4 dex as being good-quality observations. At lower signal to noise, we see a bias for higher metallicities in dwarf galaxy members and applying this selection removes those bad measurements. We follow the procedure performed in (section 4 of Kirby et al. 2017) to calculate the metallicity dispersion, performing maximum likelihood estimation to fit a Gaussian distribution to the Fe/H measurements of Tri II members. We assume the existence of a Fe/H zero-point offset between the instruments, which was determined using the non-outlier offset model (setting outlier fraction to zero in equation 2) with the two stars that are in the overlap of the MMT and Keck catalogs, *Star46* and *Star40*. We find an offset of -0.63 ± 0.20 dex to be added to the Kirby et al. (2017) metallicities. We note that a weighted mean is not the preferred way of combining metallicity measurements and improvements to signal to noise would be achieved by co-adding the relevant spectra. Fig. C1 shows Fe/H

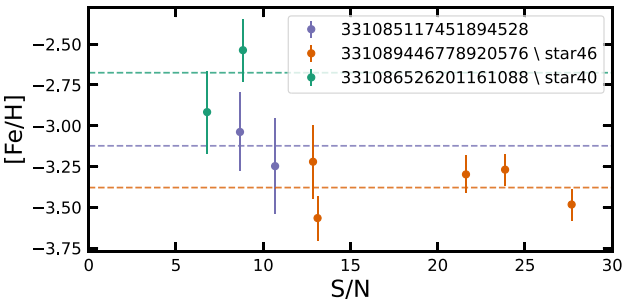

Figure C1. Fe/H measurements v. signal to noise of the Tri II members in our MMT catalog, coloured by object. The dotted lines mark the corresponding weighted mean Fe/H values for each star. This plot shows only the MMT measurements that survive our quality cut and are subsequently used in our metallicity dispersion calculation.

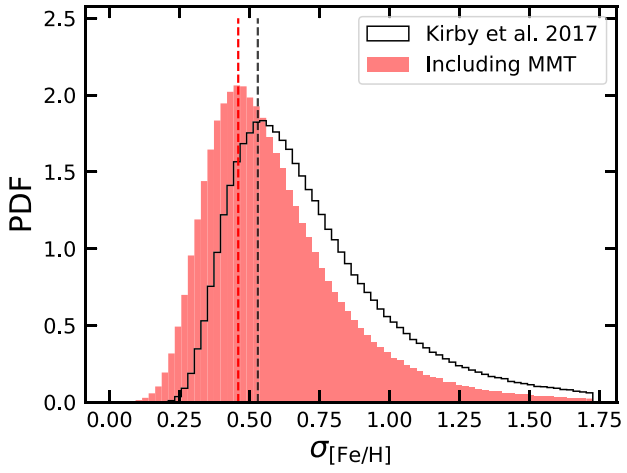

Figure C2. Metallicity dispersion likelihood distributions calculated when using only the Keck data (Kirby et al. 2017) for Tri II (black) and when also including our Tri II MMT measurements (red). The dotted lines mark the maximum likelihood values.

measurements for the stars observed in MMT.

Kirby et al. (2017) found $\sigma([Fe/H]) = 0.53^{+0.38}_{-0.12}$ dex when including all potential member stars in their catalog [fig. 6 (b) of Kirby et al. 2017]. The effect of including the MMT observations can be seen in Fig. C2, slightly shifting the maximum likelihood value to $\sigma([Fe/H]) = 0.46^{+0.37}_{-0.09}$.

APPENDIX D: DATA TABLES

Table D1. Individual observations of Tri II members taken with MMT Hectochelle. This table is a subset of the full MMT catalog. The complete catalog is publicly available at the Zenodo database, https://doi.org/10.5281/zenodo.6561483.

Gaia ID	KCS2015	MIC2016	Member	RA (ICRS)	Dec. (ICRS)	HJD (d)	S/N	v_{los} (km s^{-1})	[Fe/H]	T_{eff}	log g
3310851174518945 28			True	33.4272917	36.0950281	2457683.72	8.67	− 386.9 ± 0.7	− 3.0 ± 0.3	4760 ± 226	0.7 ± 0.5
3310851174518945 28			True	33.4272917	36.0950281	2457688.77	10.68	− 385.5 ± 0.9	− 3.2 ± 0.4	4684 ± 255	1.4 ± 0.5
3310851174518945 28			True	33.4272917	36.0950281	2457711.69	6.07	− 384.4 ± 1.7	− 3.2 ± 0.6	4772 ± 453	0.9 ± 0.7
3310851174518945 28			True	33.4272917	36.0950281	2457685.74	4.74	− 383.4 ± 1.7	− 3.0 ± 0.7	4783 ± 495	1.7 ± 0.9
3310865262011610 88	65	46	True	33.33975	36.1659431	2457374.8	8.84	− 400.4 ± 0.7	− 2.5 ± 0.3	4823 ± 159	2.0 ± 0.4
3310865262011610 88	65	46	True	33.33975	36.1659431	2457683.72	6.78	− 405.9 ± 0.8	− 2.9 ± 0.3	4535 ± 215	0.9 ± 0.4
3310865262011610 88	65	46	True	33.33975	36.1659431	2457688.77	5.08	− 405.1 ± 1.0	− 2.0 ± 0.7	5416 ± 588	2.0 ± 0.7
3310865262011610 88	65	46	True	33.33975	36.1659431	2457711.69	2.88	− 386.4 ± 2.1	− 0.8 ± 0.9	6811 ± 855	2.2 ± 1.0
3310894467789205 76	106	40	True	33.3189583	36.17939	2457374.8	27.68	− 382.8 ± 0.6	− 3.5 ± 0.1	4367 ± 87	0.9 ± 0.2
3310894467789205 76	106	40	True	33.3189583	36.17939	2457683.72	21.62	− 381.8 ± 0.5	− 3.3 ± 0.2	4507 ± 95	1.0 ± 0.3
3310894467789205 76	106	40	True	33.3189583	36.17939	2457688.77	23.86	− 381.9 ± 0.5	− 3.3 ± 0.1	4505 ± 82	0.8 ± 0.2
3310894467789205 76	106	40	True	33.3189583	36.17939	2457711.69	13.11	− 381.9 ± 0.7	− 3.6 ± 0.2	4253 ± 135	0.7 ± 0.3
3310894467789205 76	106	40	True	33.3189583	36.17939	2457685.74	12.85	− 382.2 ± 0.8	− 3.2 ± 0.3	4597 ± 195	1.1 ± 0.5

Table D2. Individual observations of Tri II members from Keck DEIMOS used in this analysis after adding a $\delta_v = -1.33$ km s^{-1} zero-point offset correction. The first epochs for each star are listed with the star's ID numberings and sky position while any additional epochs for the same star are in subsequent rows with '-' in the ID and sky position columns.

KCS2015	MIC2016	RA (ICRS)	Dec. (ICRS)	HJD (d)	v_{los}(km s^{-1})
N/A	8	33.2591667	36.2090836	2457284.07	− 388.4 ± 7.7
128	N/A	33.3093333	36.1641944	2457303.10	− 386.3 ± 3.2
–	–	–	–	2457416.70	− 385.4 ± 2.1
–	–	–	–	2457416.80	− 384.2 ± 2.0
–	–	–	–	2457639.10	− 383.8 ± 2.1
N/A	31	33.4694167	36.2233611	2457370.70	− 377.6 ± 1.8
–	–	–	–	2457416.70	− 381.5 ± 2.6
–	–	–	–	2457639.10	− 377.0 ± 2.8
–	–	–	–	2457284.07	− 377.1 ± 3.1
N/A	29	33.3789583	36.1988889	2457370.70	− 387.5 ± 4.7
–	–	–	–	2457284.07	− 398.4 ± 7.8
N/A	27	33.3389583	36.1414167	2457370.70	− 373.5 ± 5.2
–	–	–	–	2457416.70	− 389.9 ± 8.3
–	–	–	–	2457284.07	− 402.7 ± 6.6
N/A	26	33.3534583	36.1727222	2457370.70	− 376.9 ± 11.2
N/A	24	33.3416667	36.1738611	2457416.70	− 371.8 ± 17.1
–	–	–	–	2457284.07	− 384.4 ± 4.9
76	23	33.3358750	36.1629167	2457303.10	− 391.0 ± 3.0
–	–	–	–	2457370.70	− 384.6 ± 3.1
–	–	–	–	2457639.10	− 384.0 ± 3.0
–	–	–	–	2457284.07	− 389.2 ± 3.6
N/A	22	33.3028750	36.1470556	2457370.70	− 381.5 ± 3.4
–	–	–	–	2457416.70	− 381.4 ± 3.3
–	–	–	–	2457416.80	− 384.9 ± 3.7
–	–	–	–	2457569.10	− 381.1 ± 23.5
–	–	–	–	2457639.10	− 376.6 ± 6.6
–	–	–	–	2457284.07	− 388.3 ± 3.8
116	21	33.3165000	36.1710556	2457303.10	− 378.9 ± 3.7
–	–	–	–	2457370.70	− 383.3 ± 2.3
–	–	–	–	2457416.70	− 387.0 ± 3.2
–	–	–	–	2457416.80	− 382.5 ± 3.6
–	–	–	–	2457639.10	− 380.6 ± 3.1
–	–	–	–	2457284.07	− 384.1 ± 3.1
91	20	33.3305000	36.1925833	2457303.10	− 387.3 ± 3.1
–	–	–	–	2457370.70	− 379.1 ± 1.9
–	–	–	–	2457569.10	− 388.2 ± 3.9
–	–	–	–	2457639.10	− 379.2 ± 2.4
–	–	–	–	2457284.07	− 380.0 ± 2.9
N/A	9	33.3639183	36.2251930	2457416.70	− 388.9 ± 7.7
–	–	–	–	2457284.07	− 406.0 ± 5.1
106	40	33.3189583	36.1793889	2457303.10	− 383.6 ± 1.5
–	–	–	–	2457416.70	− 382.1 ± 1.5
–	–	–	–	2457416.80	− 383.3 ± 1.5
–	–	–	–	2457569.10	− 382.8 ± 1.5
–	–	–	–	2457284.07	− 380.5 ± 2.3
65	46	33.3397500	36.1659444	2457303.10	− 375.8 ± 1.7
–	–	–	–	2457416.70	− 386.7 ± 1.6
–	–	–	–	2457569.10	− 376.3 ± 4.0
–	–	–	–	2457639.10	− 384.6 ± 1.6
–	–	–	–	2457284.07	− 373.8 ± 2.4

This paper has been typeset from a TEX/LATEX file prepared by the author.